Mon. Not. R. Astron. Soc. **000**, 1–12 (2015) Printed 24 August 2015 (MN LaTeX style file v2.2)

Luminosity function of [OII] emission-line galaxies in the MassiveBlack-II simulation

KwangHo Park[1,2]⋆, Tiziana Di Matteo[1]⋆, Shirley Ho[1]⋆, Rupert Croft[1], Stephen M. Wilkins[3], Yu Feng[1,4] and Nishikanta Khandai[5,6]

[1] *McWilliams Center, Carnegie Mellon University, Pittsburgh, PA 15213, USA*
[2] *Center for Relativistic Astrophysics, Georgia Institute of Technology, Atlanta, GA 30332, USA*
[3] *Astronomy Centre, Department of Physics and Astronomy, University of Sussex, Brighton BN1 9QH, UK*
[4] *Berkeley Center for Cosmological Science, CA 94720, USA*
[5] *Brookhaven National Laboratory, Department of Physics, Bldg 510, Upton, NY 11973, USA*
[6] *National Institute of Science Education and Research, Sachivalay Marg, PO Sainik School, Bhubaneswar-751005, Odisha, India*

Accepted. Received 2015

ABSTRACT

We examine the luminosity function (LF) of [OII] emission-line galaxies in the high-resolution cosmological simulation MassiveBlack-II (MBII). From the spectral energy distribution of each galaxy, we select a sub-sample of star-forming galaxies at $0.06 \leqslant z \leqslant 3.0$ using the [OII] emission line luminosity L([OII]). We confirm that the specific star formation rate matches that in the GAMA survey. We show that the [OII] LF at $z = 1.0$ from the MBII shows a good agreement with the LFs from several surveys below L([OII])=$10^{43.0}$ erg s^{-1} while the low redshifts ($z \leqslant 0.3$) show an excess in the prediction of bright [OII] galaxies, but still displaying a good match with observations below L([OII])=$10^{41.6}$ erg s^{-1}. Based on the validity in reproducing the properties of [OII] galaxies at low redshift ($z \leqslant 1$), we forecast the evolution of the [OII] LF at high redshift ($z \leqslant 3$), which can be tested by upcoming surveys such as the HETDEX and DESI. The slopes of the LFs at bright and faint ends range from -3 to -2 showing minima at $z = 2$. The slope of the bright end evolves approximately as $(z+1)^{-1}$ at $z \leqslant 2$ while the faint end evolves as $\sim 3(z+1)^{-1}$ at $0.6 \leqslant z \leqslant 2$. In addition, a similar analysis is applied for the evolution of [OIII] LFs, which is to be explored in the forthcoming survey WFIRST-AFTA. Finally, we show that the auto-correlation function of [OII] and [OIII] emitting galaxies shows a rapid evolution from $z = 2$ to 1.

Key words: cosmology: theory – galaxies: evolution – galaxies: luminosity function, mass function – stars: formation – methods: numerical.

1 INTRODUCTION

Understanding the star formation history of the Universe is essential in decoding the evolution and mass assembly of galaxies (Lilly et al. 1996; Madau et al. 1996; Hopkins 2004; Hopkins & Beacom 2006). Observations of star-forming galaxies at high redshift reveal that the cosmic star formation rate (SFR) density has been decreasing since reaching the peak at $z \sim 2$ (Madau et al. 1996; Hopkins & Beacom 2006; Kennicutt & Evans 2012). Thus, interpreting the evolution of the global SFR around this redshift ($z \sim 2$) has been one of the main interests in the astrophysics community. In particular, the role of self-regulated processes of star formation and the effect of feedback by accretion on to supermassive black holes (SMBH) at the centres of galaxies have been the main clues in deciphering the observed star formation history.

The SFR of an individual galaxy is estimated using several indicators such as nebular emission lines or the UV continuum. Both indicators are directly linked to the ionizing flux from young massive stars, whereas the flux in the mid-infrared (MIR) or far-infrared (FIR) are used to trace the re-radiated emission by dust. Among the star formation indicators, Hα is regarded as one of the best direct indicators of the current SFR since the line strength of Hα is a good tracer of the photo-ionized gas around massive young stars (< 20 Myr) (Kennicutt 1998). However, due to the rest-frame wavelength ($\lambda_{\mathrm{H}\alpha} = 6563$ Å), it is challenging to use Hα for galaxies at high redshift ($z > 1$) since the observed wavelength is redshifted to a wavelength longer than NIR ($\lambda_{\mathrm{obs}} > 1$ µm), which is difficult to observe from the ground. In contrast, [O II] $\lambda\lambda 3726, 3729$ emission line doublet can still be observed from the ground in the wavelength $\lambda_{\mathrm{obs}} < 1$ µm for galaxies at high redshift ($z < 1.6$) (Gallego et al. 2002; Ly et al. 2007; Gilbank et al. 2010; Zhu, Moustakas & Blanton 2009; Ciardullo et al. 2013; Comparat et al. 2015). Since the [O II] line luminosity L([OII]) is an indirect indicator (un-

⋆ E-mail: kwangho.park@physics.gatech.edu (KP); tiziana@phys.cmu.edu (TDM); shirleyh@andrew.cmu.edu (SH)

like Hα), it requires an extensive calibration based on the properties of the galaxies such as the metallicity and stellar mass (M_*) (Kewley, Geller & Jansen 2004; Moustakas, Kennicutt & Tremonti 2006; Gilbank et al. 2010). At even higher redshift ($z > 2$), one can use the UV continuum, which also directly traces the ionizing photons, but it measures the SFR over longer timescales (~ 100 Myr).

Over the past few decades, systematic searches for emission-line galaxies (ELGs) have been made. Gilbank et al. (2010) explored the SFR at $z \sim 0.1$ using [O II], Hα and u-band luminosities from the deep 275 deg^2 Stripe 82 field in the Sloan Digital Sky Survey (SDSS) coupled with UV data from the Galaxy Evolution EXplorer (GALEX) satellite. Also, the pilot survey of the Hobby-Eberly Telescope Dark Energy Experiment (HETDEX; Adams et al. 2011; Ciardullo et al. 2013) observed 284 [O II] emitting galaxies at $z < 0.56$ in 169 arcmin^2. The HETDEX pilot survey is a blind integral-field spectroscopic study of four data-rich areas of sky: COSMOS (Scoville et al. 2007), GOODS-N (Giavalisco et al. 2004), MUNICS-S2 (Drory et al. 2001), and XMM-LSS (Pierre et al. 2004). The Galaxy And Mass Assembly survey (GAMA; Bauer et al. 2013) also targets $\sim 73,000$ galaxies at $0.05 < z < 0.32$ with $M_* < 10^{10}$ M$_\odot$. The GAMA survey calculates the SFR using the Hα emission line and explores how the specific SFR (sSFR) depends on the stellar mass of the galaxies. Recently, Comparat et al. (2015) explored the evolution of the luminosity function (LF) of the [O II] emitters in the redshift range $0.1 < z < 1.65$ based on the medium-resolution flux-calibrated spectra of ELGs with the VLT/FORS2 instrument and the SDSS-III/BOSS spectrograph. In the forthcoming years, there are ambitious surveys targeting ELGs at high redshift. The Dark Energy Spectroscopic Instrument (DESI) is a multi-fiber spectrograph that will target 18 million ELGs (Schlegel et al. 2009; Levi et al. 2013). DESI aims to probe the effect of the dark energy on the expansion history of the Universe using baryon acoustic oscillations (BAO) with a sky coverage of 14,000–18,000 deg^2. Another survey is the space-based Wide-Field InfraRed Survey Telescope-Astrophysics Focused Telescope Assets (WFIRST-AFTA) which will perform a deep infrared survey of $2400\,\mathrm{deg}^2$ and obtain spectroscopic redshifts of galaxies targeting 20 million Hα emitters at $1 < z < 2$ and 2 million [O III] ELGs at $2 < z < 3$ (Spergel et al. 2013).

In cosmological simulations, it is challenging to study stellar mass assembly of individual galaxies as it requires a high resolution and a large volume at the same time. A sufficiently large volume is needed for statistically meaningful results whereas high resolution properly manifests baryonic physics related to star formation and black hole (BH) feedback. It is also difficult to evolve a simulated universe up to the present ($z \sim 0$). Considering all these numerical challenges, the *MassiveBlack-II* simulation (MBII; Khandai et al. 2015), which is a successor to the *MassiveBlack* simulation (Di Matteo et al. 2012), is one of the unique simulations in that it is a state-of-the-art high resolution cosmological hydrodynamical simulation with a large comoving volume (c.f., Vogelsberger et al. 2014; Schaye et al. 2015).

In this paper, we investigate the properties of the star-forming galaxies in the MBII simulation, which are selected by the [O II] and [O III] emission-line luminosity in the generated spectral energy distributions (SEDs). The main goal of this study is to validate whether the star-forming galaxies in the high-resolution cosmological simulation can reproduce results from recent surveys for the [O II] emitting galaxies and make a prediction for the upcoming surveys that target the high redshift [O II] emitters. In Section 2 we explain how we select the [O II] emitting galaxies from the synthesised SEDs and compare the properties of the selected samples with observations. In Section 3, we compare the LFs from the simulation and observation at $0.1 \leqslant z \leqslant 1.0$, and make a prediction for the LF of the [O II] emitting (and [O III]) galaxies at high redshift. We also present the evolution of the auto-correlation function of the [O II] ELGs at $z \leqslant 4$. Finally, we summarise and discuss the results in Section 4.

2 METHODS

2.1 The MassiveBlack-II simulation

We use the state-of-the-art high resolution hydrodynamical simulation MBII (Khandai et al. 2015) performed with the hybrid version TreePM-SPH code P-GADGET designed for running on PETAFLOP-scale supercomputer facilities. The MBII contains $N_{\rm part} = 2 \times 1792^3$ dark matter and gas particles in a comoving volume of $(100\ h^{-1}{\rm Mpc})^3$ to satisfy the needs of large volume and high resolution at the same time. In the MBII simulation, the ΛCDM universe is evolved from $z = 159$ to $z = 0.06$ with a high mass resolution of $1.1 \times 10^7\ h^{-1}{\rm M}_\odot$ for dark matter and $2.2 \times 10^6\ h^{-1}{\rm M}_\odot$ for gas particles with a smoothing length of $1.85\ h^{-1}$kpc. The cosmological parameters used in the MBII are: $\sigma_8 = 0.816$, spectral index $n_s = 0.968$, matter density fraction of the critical density $\Omega_{\rm m} = 0.275$, vacuum energy density fraction $\Omega_\Lambda = 0.725$, baryon density fraction $\Omega_{\rm b} = 0.046$, and Hubble constant $h = 0.702$ from the 7-year Wilkinson Microwave Anisotropy Probe (Komatsu et al. 2011).

The MBII includes a sub-grid model for star-forming multi-phase gas (Springel & Hernquist 2003). In this model, a thermal instability takes place at a critical density threshold creating a multi-phase medium consisting of cold clouds in pressure equilibrium with surrounding hot gas. A star formation prescription is given by the Kennicutt-Schmidt law (Kennicutt 1989), where the SFR is proportional to the density of cold clouds (i.e., $\rho_{\rm SFR} \propto \rho_{\rm gas}^N$ where $N = 1.5$ is adopted). Gas particles are converted to star particles according to the star formation prescription. Star formation is then regulated by the supernovae feedback, which heats the surrounding gas and creates a self-regulated cycle.

In the MBII, a BH is introduced as a collisionless sink particle in a newly collapsing halo identified by the friends-of-friends halo-finder on-the-fly at a regular time interval. A seed BH with mass $M_{\rm seed} = 5 \times 10^5\ h^{-1}{\rm M}_\odot$ is inserted into a halo with mass $M_{\rm halo} \geqslant 5 \times 10^{10}\ h^{-1}{\rm M}_\odot$. After seeded, BHs are assumed to grow at the Bondi-Hoyle rate (Bondi & Hoyle 1944; Bondi 1952) $\dot{M}_{\rm BH} = 4\pi G^2 \rho_\infty M_{\rm BH}^2 (c_{s,\infty}^2 + v_{\rm BH}^2)^{-3/2}$, where $v_{\rm BH}$ is the velocity of the BH relative to the surrounding gas, and ρ_∞ and $c_{s,\infty}$ are the density and sound speed of the gas in the multi-phase state (Pelupessy, Di Matteo & Ciardi 2007). The accretion rate is limited by $2 \times \dot{M}_{\rm Edd}$ (Begelman, Volonteri & Rees 2006; Volonteri & Rees 2006) where $\dot{M}_{\rm Edd}$ is the Eddington accretion rate. The accretion rate is converted to a bolometric luminosity $L_{\rm bol} = \eta \dot{M}_{\rm BH} c^2$, where η is the radiative efficiency and we adopt the standard value of 0.1 for a thin disk model (Shakura & Sunyaev 1973). It is also assumed that 5 per cent of the BH luminosity thermally couples with the surrounding gas, isotropically depositing the radiation energy to the gas particles within the BH kernel (64 nearest neighbours) to match the observed $M_{\rm BH}$–σ relation (Di Matteo, Springel & Hernquist 2005; Springel, Di Matteo & Hernquist 2005). The current BH growth model has been adopted in extensive studies (Li et al. 2007; Sijacki et al. 2007; Di Matteo et al. 2008; Colberg & Di Matteo 2008; Croft et al. 2009; Degraf, Di Matteo & Springel 2010,

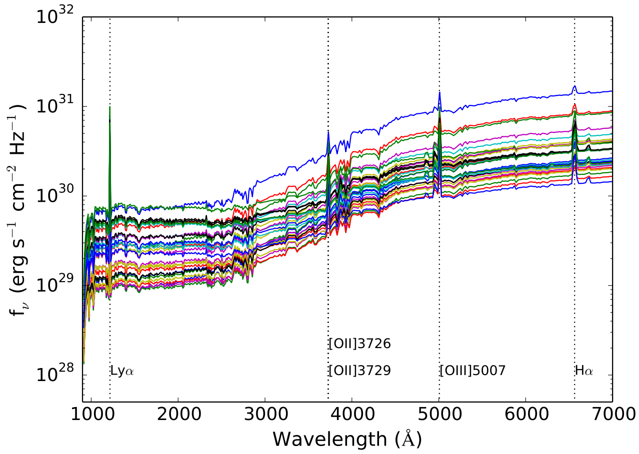

Figure 1. Examples of the spectral energy distribution of 20 star-forming galaxies in the range $10 < \mathrm{SFR}\ (\mathrm{M}_\odot\ \mathrm{yr}^{-1}) < 100$ at $z = 0.1$ in the MBII simulation. The stellar continuum and nebular emission lines are generated from the star formation history of each galaxy using the stellar population synthesis code PEGASE.2. Note that the nebular emission lines such as Lyα, [O II] $\lambda\lambda$3726, 3729, [O III] λ5007, and Hα are distinct.

2011; Degraf et al. 2011; Di Matteo et al. 2012; DeGraf et al. 2012; Chatterjee et al. 2012; Feng et al. 2014). BHs are assumed to merge when one BH enters within the kernel of another BH with a relative velocity below the local gas sound speed.

2.2 [OII] emission-line galaxies in the MBII

The high resolution of the MBII enables us to generate a SED of an individual galaxy. We adopt the previous work by Wilkins et al. (2013b) to generate the SEDs and we briefly explain the process in this section.

2.2.1 Generating SEDs with emission lines

The stellar population synthesis code PEGASE.2 (Fioc & Rocca-Volmerange 1997, 1999) is used to generate SEDs of individual star particles as a function of the stellar mass, age, and metallicity and assuming the Salpeter initial mass function. We then calculate hydrogen line fluxes first using the PEGASE.2 while non-hydrogen line fluxes are estimated from hydrogen lines using the metallicity-dependent conversion by Anders & Fritze-v. Alvensleben (2003). These nebular emission lines, reprocessed ionizing radiation by interstellar medium, include Lyα, [O II] $\lambda\lambda$3726, 3729, [O III] λ5007, and Hα. The rest-frame SEDs of galaxies are generated by integrating all the SEDs of star particles and emission lines with a wavelength resolution of 20 Å (Wilkins et al. 2013b,a). For a galaxy with a stellar mass $M_* = 10^9\ h^{-1}\mathrm{M}_\odot$, for example, $\sim$450 SEDs from individual star particles are integrated to produce the SED of the galaxy. Fig. 1 shows 20 randomly selected examples of synthesised SEDs of star-forming galaxies with $10 <$ SFR $(\mathrm{M}_\odot\ \mathrm{yr}^{-1}) < 100$ at $z = 0.1$. Note that the nebular emission lines, such as Lyα, [O II], [O III], and Hα, are clearly visible for these star-forming galaxies.

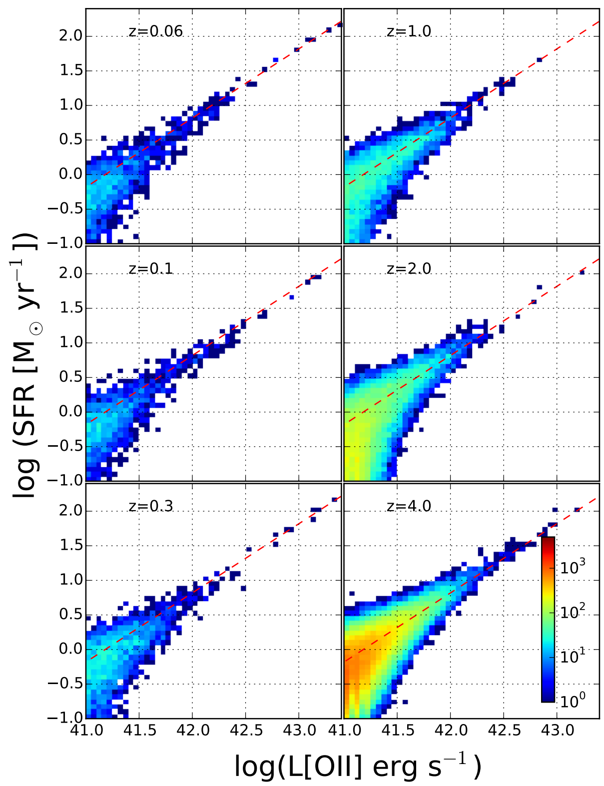

Figure 2. 2D histogram of the [O II] luminosity and the SFR in the MBII for different redshifts (z =0.06, 0.1, 0.3, 1.0, 2.0 and 4.0). The dashed line in each panel shows the empirical relationship from Kewley, Geller & Jansen (2004), which shows a good agreement with the MBII simulation. The galaxies with higher SFR show a tight match while the scatter increases as the L([O II]) decreases.

2.2.2 Selecting [OII] emission-line galaxies from SEDs

We select a sample of [O II] ELGs using the generated SED for each galaxy. The flux of [O II] emission line for an individual galaxy is calculated from the SED by mimicking observation. We apply a simple criterion $\mathrm{L}_{\lambda3730}/\mathrm{L}_{\mathrm{cont}} > 1$, where $\mathrm{L}_{\mathrm{cont}}$ is the estimated flux of the continuum at λ3730 by averaging the fluxes at the neighbouring wavelengths. This method selects galaxies with positive flux at the [O II] emission line wavelength. Then the luminosity of the [O II] emission line component is obtained by subtracting the estimated continuum as L([O II]) = $\mathrm{L}_{\lambda3730} - \mathrm{L}_{\mathrm{cont}}$. We check that this simple method recovers the original line [O II] luminosity well (see Appendix A).

2.2.3 Comparison with L([OII])–SFR empirical relation

Fig. 2 shows the relation between L([O II]) and SFR of the [O II] ELGs at redshifts $z = 0.06$, 0.1, 0.3, 1.0, 2.0, and 4.0. The MBII simulation displays a good agreement with the empirical relationship by Kewley, Geller & Jansen (2004),

$$\mathrm{SFR}\ (\mathrm{M}_\odot\ \mathrm{yr}^{-1}) = \frac{\mathrm{L([O\ II])}}{1.52 \times 10^{41}} (\mathrm{erg\ s}^{-1}), \qquad (1)$$

which is shown as a dashed line in each panel. In general, the galaxies with higher SFRs show a better agreement with the em-

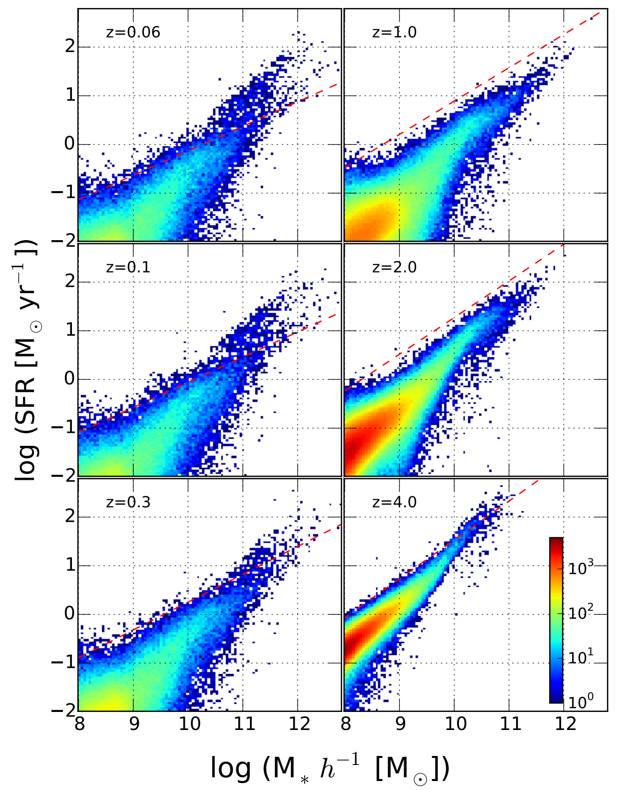

Figure 3. 2D histogram for the distribution of SFR and stellar mass (M_*) of galaxies in the MBII at the redshift z =0.06, 0.1, 0.3, 1.0, 2.0 and 4.0, respectively. Most of the star-forming galaxies with $M_* \geqslant 10^9\ h^{-1}\mathrm{M}_\odot$ at $z = 0.06$ are not selected by the L([O II]) while most of the star-forming galaxies with the same stellar mass at $z = 4.0$ are selected. The dashed line for each redshift is from Speagle et al. (2014).

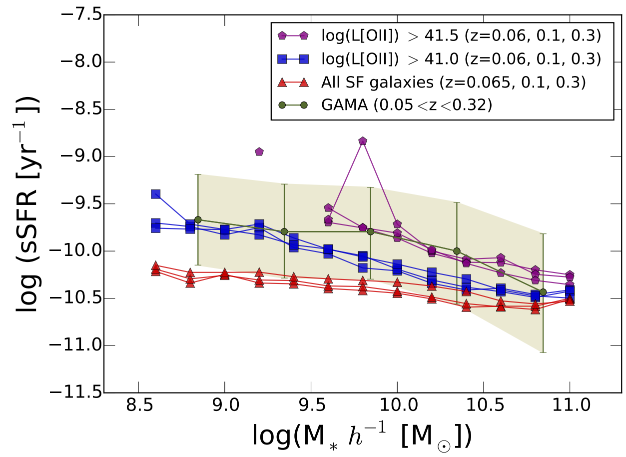

Figure 4. Specific star formation rate (sSFR) as a function of the stellar mass ($M_*/\mathrm{M}_\odot$) at $z = 0.06, 0.1$, and 0.3. Different symbols are used for different luminosity cuts: triangles are all star-forming galaxies, squares are galaxies with L([O II]) $\geqslant 10^{41.0}$ erg s^{-1}, and pentagons are galaxies with L([O II]) $\geqslant 10^{41.5}$ erg s^{-1}. The shaded region shows the mean sSFR with scatter from the GAMA survey (Bauer et al. 2013) at $0.05 < z < 0.32$ as a function of the stellar mass in the range $9.0 < \log\,(M_*\ [\mathrm{M}_\odot]) < 11.0$.

pirical relation while the scatter increases as L([O II]) decreases. Due to the mass resolution of star particles in the MBII (i.e., $m_* = 2.2 \times 10^6\ h^{-1}\mathrm{M}_\odot$), shot noise starts to dominate for the sample of galaxies with L([O II]) $\leqslant 10^{40.6}$ erg s^{-1} (see Appendix A for details). The current SFR is not well represented in L([O II]) below this luminosity cut, which sets the lower limit of L([O II]) for our current study. This luminosity cut can be translated to a SFR of $\sim$0.3 M$_\odot$ yr^{-1} using equation (1).

Fig. 3 shows the distribution of the stellar mass (M_*) and SFRs of all star-forming galaxies in the MBII for redshifts z =0.06, 0.1, 0.3, 1.0, 2.0 and 4.0. In general, the SFR is proportional to the stellar mass M_* for each redshift, and the SFR for a given stellar mass increases as we go to high redshift. Note that the number of stellar particles is $\sim$450 for a galaxy with stellar mass $M_* \sim 10^9\ h^{-1}\mathrm{M}_\odot$. When the luminosity cut mentioned above is applied (i.e., SFR of $\sim$ 0.3 M$_\odot$ yr^{-1}), it removes a large fraction of galaxies at low stellar mass while the sample of star-forming galaxies is more complete for massive galaxies. The average stellar mass of galaxies selected this way is approximately $M_* \geqslant 10^{10}\ h^{-1}\mathrm{M}_\odot$ at $z = 0.06$. The completeness at a given stellar mass also depends on redshift. For example, most of the star-forming galaxies with $M_* \sim 10^9\ h^{-1}\mathrm{M}_\odot$ at $z = 0.06$ are not selected for our luminosity cut while most of the star-forming galaxies with the same stellar mass are selected at $z = 4.0$.

For comparison, the observed relation between the SFR and the galaxy stellar mass from Speagle et al. (2014)

$$\log \mathrm{SFR}(M_*, t) = (0.84 \pm 0.02 - 0.026 \pm 0.003 \times t) \log M_* - (6.51 \pm 0.24 - 0.11 \pm 0.03 \times t) \tag{2}$$

where t is the age of the universe in Gyr, is overplotted in Fig. 3. Since it is known that the MBII produces too many galaxies at low and high stellar mass (Khandai et al. 2015), it is expected that the overabundance in stellar mass function inevitably propagates into the [O II] LF. The excess is obviously seen in Fig. 3 at low redshifts.

2.2.4 *Specific star formation rate*

In this section, we compare the SFR per stellar mass (i.e., sSFR=SFR/M_*) of the [O II] emitters with the GAMA survey (Bauer et al. 2013). Fig. 4 shows the average sSFR as a function of the stellar mass in the range $9.0 < \log(M_*\ [\mathrm{M}_\odot]) < 11.0$ for redshifts $z = 0.06$, 0.1, and 0.3 with different L([O II]) cuts. Triangles are all star-forming galaxies, squares are galaxies with L([O II]) $\geqslant 10^{41.0}$ erg s^{-1}, and pentagons are galaxies with L([O II]) $\geqslant 10^{41.5}$ erg s^{-1}. The shaded region in Fig. 4 shows the observed average sSFR with scatter from the GAMA survey. The mean sSFR increases with higher luminosity cuts and the sSFR with the luminosity cut of $10^{41.5}$ erg s^{-1} matches well with the GAMA survey. However, this luminosity cut removes galaxies with $M_* \leqslant 10^{10}$ M$_\odot$. The simulation converges to the result of GAMA survey with increasing luminosity cut, but the halos with stellar mass $M_* < 10^{10}$ M$_\odot$ are lost with this luminosity cut (L([O II]) $\geqslant 10^{41.5}$ erg s^{-1}).

2.2.5 *Possible contamination from active galactic nuclei*

In our scheme, the SED of a galaxy does not include the emission lines from the hot ionized gas produced by active galactic nuclei (AGN). We assume that the whole [O II] emission line flux originates from SFR. AGN contamination to [O II] line certainly affects

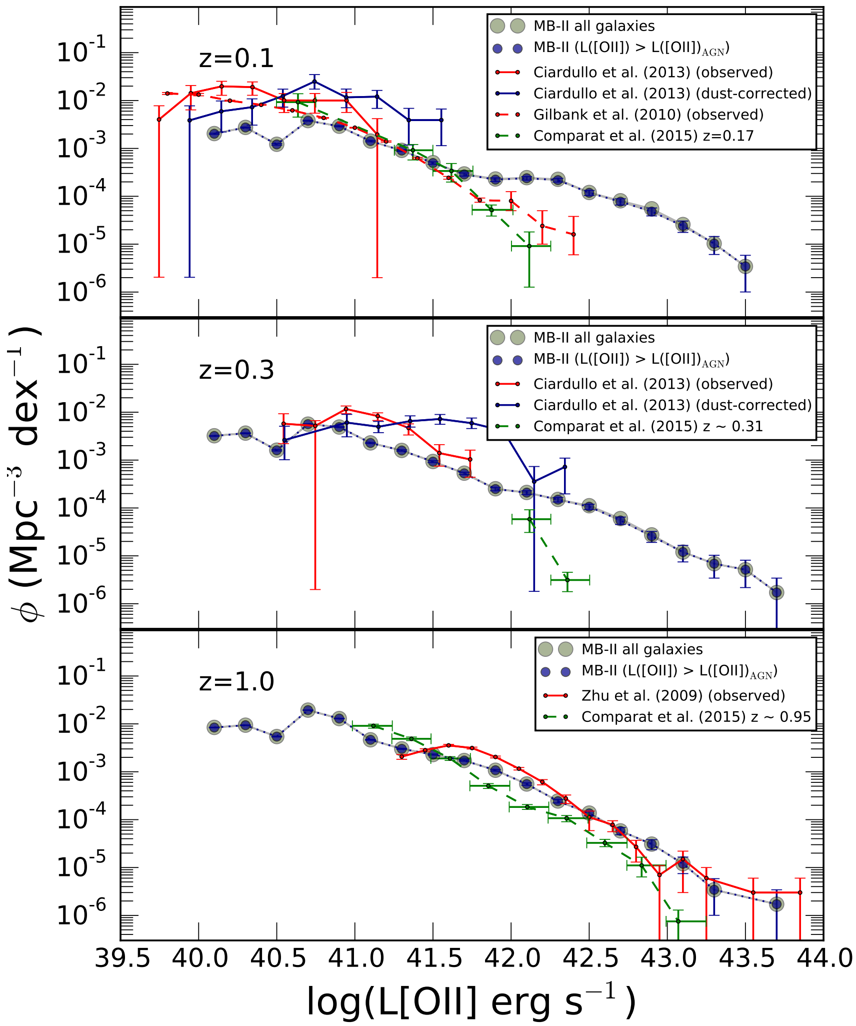

Figure 5. Comparison of the LFs of the [O II] emitting galaxies in the MBII simulation at $z = 0.1$ (top), 0.3 (middle), and $z = 1.0$ (bottom) with the observations. Big circles show the [O II]-selected sample in the MBII simulation and the small circles along with the Poisson errors show the samples with AGNs excluded using the method mentioned in Section 2.2.5 to avoid the possible contamination of AGNs. There is no severe contamination to the [O II] emission line. Red (observed) and blue (dust-corrected) solid lines at $z = 0.1$ and 0.3 are from HETDEX pilot survey (Ciardullo et al. 2013) while the red dashed line (observed) at $z = 0.1$ shows the observation from SDSS (Gilbank et al. 2010). The LFs of the MBII show an excess in the prediction of bright [O II] emitters at L([O II]) $> 10^{41.6}$ erg s^{-1} at low redshift ($z \leqslant 0.3$). At $z = 1.0$, the LF matches well with the DEEP2 observation (Zhu, Moustakas & Blanton 2009) and Comparat et al. (2015) below L([O II])=$10^{43.0}$ erg s^{-1}.

the estimation of the SFR of a galaxy, but observations show that the level of actual contamination is not high (e.g., Bauer et al. 2013; Zhu, Moustakas & Blanton 2009).

However, we exclude galaxies that might potentially contaminate our samples when the AGN-associated [O II] emission line is added to the current SEDs. We only select galaxies where the [O II] luminosity from star formation is larger than that from the AGN as L([O II])$_{\rm AGN} \leqslant$ L([O II])$_{\rm SF}$. From the accretion rate of the SMBHs for each galaxy, we calculate the bolometric luminosity of the AGN as $L_{\rm AGN} = \eta \dot{M}_{\rm BH} c^2$ where c is the speed of light and we assume the radiative efficiency $\eta = 0.1$. The direct relation between $L_{\rm AGN,bol}$ and L([O II]) is unclear, so we use the results by Heckman et al. (2004) and Netzer (2009) where the [O III]λ5007 is used as a proxy for the bolometric luminosity of the AGN $L_{\rm AGN,bol}$ and the average relation is shown as $L_{\rm AGN,bol}/L_{\rm AGN,[O\,III]} \sim$ 3500. Since the line ratio between [O II] and [O III] in AGNs ranges from 0.1–5 depending on the types (Blandford et al. 1990), we can roughly obtain the fraction of the L([O II]) out of the bolometric luminosity as $3 \times 10^{-5} \leqslant$ L([O II])$_{\rm AGN}$/L$_{\rm AGN,bol} \leqslant 0.001$.

2.2.6 Dust extinction effect

In this section, we briefly discuss the effect of the dust extinction on the L([O II]) even though we rather use the intrinsic L([O II]) without dust correction in this study. It is extremely challenging to understand the effect of the dust extinction on nebulae emission

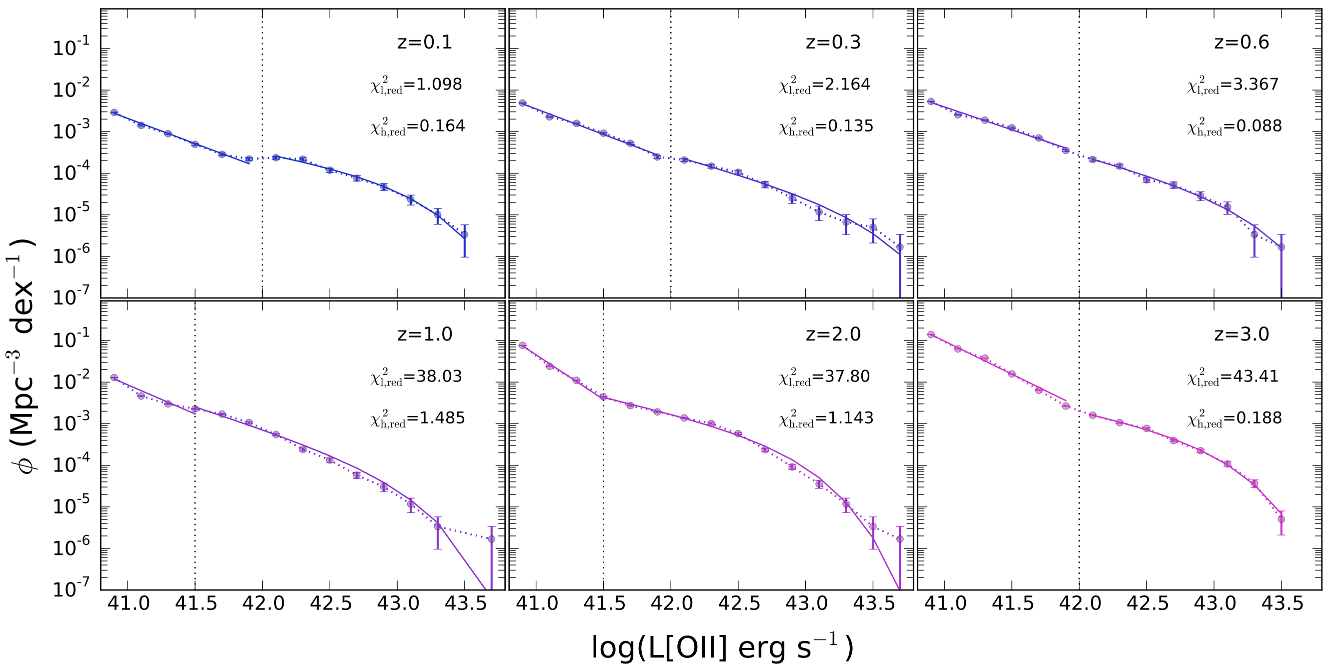

Figure 6. Fitting of LFs of the [O II] emitting galaxies at $z = 0.1$, 0.3, 0.6, 1.0, 2.0, and 3.0. For each redshift, we fit the LF with a single power-law at low luminosity and Schechter function at high luminosity. We use L([O II]) $= 10^{42.0}$ erg s^{-1} as a dividing luminosity of the fitting functions except for $z = 1.0$ and 2.0 where we apply L([O II]) $= 10^{41.5}$ erg s^{-1}, which are shown as dotted vertical lines in each panel.

lines coupled with the star formation history, metallicity, and the evolution as a function of redshift (Wilkins et al. 2013b).

Both the stellar continuum of the SEDs and emission lines are affected by the dust extinction. In observation, the internal dust extinction should be corrected to obtain the intrinsic flux at the wavelength where the emission lines are located. On the simulation side, dust-extinction effect must be added to make a direct comparison with observation. Since the wavelength $\lambda = 3730$ Å is in U band, we can apply $E(U-V)_{\rm star} = 1.64E(B-V)_{\rm star}$ to the stellar continuum. In galaxies actively forming stars, the empirical relationship of the internal dust extinction (Calzetti 2001) shows that the emission from the ionized gas suffers about twice as much reddening as the stellar continuum $E(B-V)_{\rm star} = 0.44E(B-V)_{\rm gas}$. Then the absorption in the U band becomes $A_{\rm U,gas} = A_{\rm V,gas} + (1.64A_V)/(0.44R_V)$. Applying the commonly accepted reddening coefficient $R_V \sim 3.1$ and the extinction value at V band $A_{\rm V} = 0.4$ mag from which $A_{\rm V,gas} = 0.91$ is obtained [e.g., $A_{\rm H\alpha} = 0.7^{+1.4}_{-0.7}$ for $z \sim 0.5$ galaxies (Ly et al. 2012)], the extinction coefficient of [O II] emission line is estimated as $A_{\rm [O\,II]} \sim 1.39$ mag. Therefore, the dust absorption reduces the observed [O II] line luminosity L([O II])$_{\rm o}$ to ~ 0.28 times of the intrinsic flux L([O II])$_{\rm i}$. Many studies find that the dust reddening $E(B-V)$ also depends on the intrinsic [O II] luminosity L([O II])$_{\rm i}$. For example, Kewley, Geller & Jansen (2004) measure $E(B-V) = (0.174 \pm 0.035)\log$ L([O II])$_{\rm i} - 6.84$, so the intrinsic [O II] line luminosity is expressed as L([O II])$_{\rm i}$ $= 3.11\times10^{-20}$L([O II])$_{\rm o}^{1.495}$ where the luminosities are given in unit of ergs per second.

3 RESULTS

3.1 [OII] luminosity function at low redshift

We compare the LFs of the [O II] emitting galaxies in the MBII simulation with observations at redshift $z = 0.1$, 0.3, and 1.0 from top to bottom in Fig. 5. Circles show the LFs from the MBII simulation while lines show the observational results (Zhu, Moustakas & Blanton 2009; Gilbank et al. 2010; Ciardullo et al. 2013; Comparat et al. 2015) at each redshift. Big circles show all the [O II]-selected galaxies while small circles with the Poisson errors show the galaxies with AGNs excluded to avoid a possible AGN contamination. We compare the L([O II]) with the estimated L([O II])$_{\rm AGN}$ due to AGN activity for each galaxy using the method described in Section 2.2.5. We assume that L([O II])$_{\rm AGN}$= $0.001\times$L$_{\rm AGN,bol}$ to be conservative. Note that the level of the AGN contamination in the L([O II]) LF is negligible as discussed in Section 2.2.5.

At $z = 0.1$, red (observed) and blue (dust-corrected) solid lines show HETDEX pilot survey (Ciardullo et al. 2013) while the red dashed line (observed) shows the result from SDSS (Gilbank et al. 2010). The HETDEX pilot survey has a higher number density compared to SDSS at $z = 0.1$, but the excess can be explained by the cosmic variance caused by the small sample size (< 300 galaxies at $0.1 < z < 0.56$) as discussed in Ciardullo et al. (2013). Comparat et al. (2015) matches well with other observations at low L([O II]) although it fits better with a Schechter function when the high L([O II]) samples are considered together. LFs from the MBII are a good match with the observation (Gilbank et al. 2010; Comparat et al. 2015) in the range of [O II] luminosity $10^{40.6} <$ L([O II])$< 10^{41.6}$ erg s^{-1}. The LFs of the MBII show an excess in the prediction of bright [O II] emitters at L([O II]) $> 10^{41.6}$ erg s^{-1} at low redshift ($z \leqslant 0.3$). Note that the galaxy stellar mass function (GSMF) of the MBII at low redshift is known to show

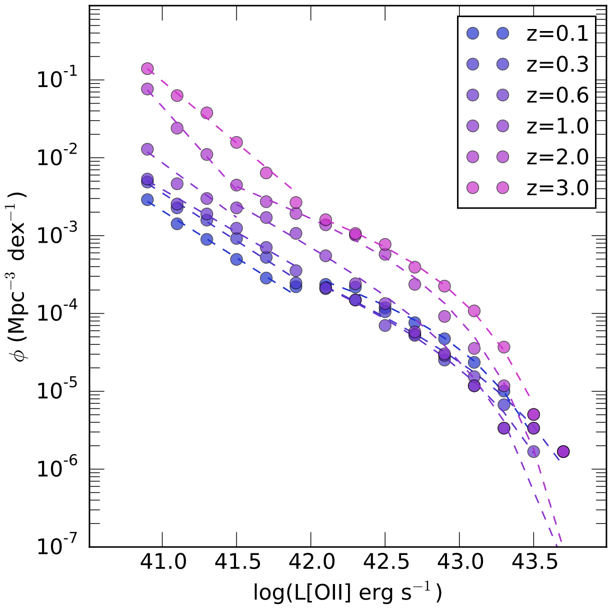

Figure 7. Evolution of the LF of the [O II] emitting galaxies from $z = 3$ to $z = 0.1$. In general, the LF increases and the slope of the LF also becomes steeper with increasing redshift. There is strong evolution of the LF for $z > 1.0$ but not below $z < 1.0$.

an excess compared to observations both in the low- and high-mass ends (Khandai et al. 2015). Since a high fraction of the star-forming galaxies in the high-mass end is selected as [O II] emitting galaxies, the overabundance in GSMF at the high-mass end is inevitably transferred to the [O II] LF.

At $z = 1.0$, the LF of the MBII shows a good match with Zhu, Moustakas & Blanton (2009) throughout the luminosity that the DEEP2 survey covers while the LF matches with Comparat et al. (2015) below L([O II])=$10^{43.0}$ erg s^{-1}, as shown at the bottom panel of Fig. 5.

3.2 Fitting function of the [OII] luminosity functions

Despite the fact that the [O II] LF is not in perfect agreement with observations at low redshift, the [O II] LF at z=1 still shows a reasonably good agreement with observations. Therefore we fit the [O II] LFs from the MBII for low redshift $z \leqslant 1.0$, and extend the fitting for LFs at high redshift in the range $1.0 < z \leqslant 3.0$. Since the exponential decline of the number density is obvious toward the high luminosity end, we use two fitting functions for lower [O II] luminosity than L([O II]) $= 10^{42}$ erg s^{-1} (dotted vertical lines) and high luminosity (L([O II]) $> 10^{42}$ erg s^{-1}), respectively. For $z = 1.0$ and 2.0, L([O II]) $= 10^{41.5}$ erg s^{-1} is used instead as the border line to adopt the fact that the Schechter function extends to lower luminosity. At low luminosity, single power-law function is used while the common Schechter (1976) function is used at high luminosity.

The Schechter function has the form

$$\phi(L)dL = \phi^* \left(\frac{L}{L^*}\right)^\alpha \exp\left(-\frac{L}{L^*}\right) d\left(\frac{L}{L^*}\right) \qquad (3)$$

where α is the slope of the faint end of the LF, L^* is the characteristic luminosity, and ϕ^* is the density of galaxies per magnitude with $L > L^*$. At low luminosity (L([O II]) $< 10^{42}$ erg s^{-1}) in each

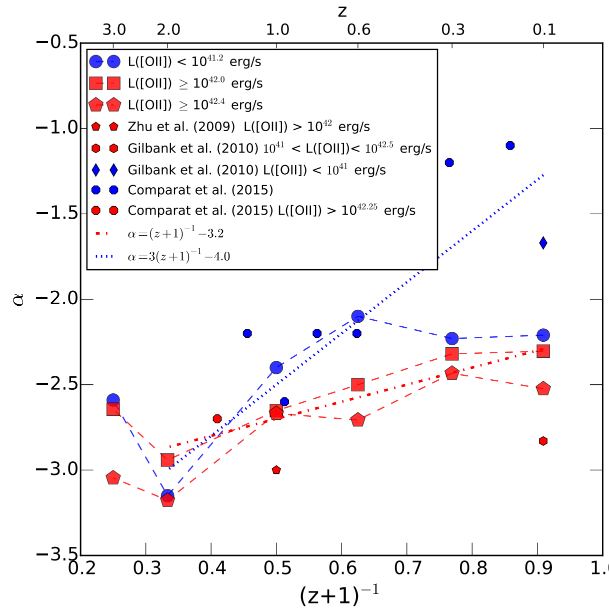

Figure 8. The slope of the LFs of the [O II] emitting galaxies as a function of redshift for the bright (squares) and faint (circles) ends. For both ends, α shows a minor change at $z \leqslant 0.3$. For the bright end, α increases approximately as $(z + 1)^{-1}$ (dot-dashed line) while α of the faint end shows the bigger change being proportional to $\sim 3(z + 1)^{-1}$ (dotted line) at high redshift $z \geqslant 0.6$. The slopes for both ends display the minima at $z = 2.0$.

redshift, a power-law fitting function is used with the form

$$\phi(\log L)d\log L = 10^{(\alpha_l+1)(\log L-42.0)+\beta_l}\, d\log L \qquad (4)$$

while the Schechter function is used for high luminosity as

$$\phi(\log L)d\log L = 10^{(\alpha_h+1)\log(\frac{L}{L^*})+\beta_h} \exp(-\frac{L}{L^*})d\log L. \qquad (5)$$

Fig. 6 shows the LFs along with fitting parameters at redshift $z = 0.1, 0.3, 0.6, 1.0, 2.0$, and 3.0, respectively. We apply Poisson errors to estimate the uncertainty of the number of galaxies in each luminosity bin (see Appendix B for the comparison of the estimated Poisson and Jackknife errors). Table 1 shows the fitting parameters and the corresponding reduced χ^2 values at different redshifts. At high luminosity ends, the number of galaxies are dominated by the Poisson errors. For example, only 2–3 galaxies are found in the simulated volume at the luminosity bin of L([O II]) $\sim 10^{43.6}$ erg s^{-1}. However, at the low luminosity ends, the small Poisson errors due to the high number of galaxies (e.g., $\sim$ 73000 galaxies at the luminosity bin L([O II]) $\sim 10^{40.8}$ erg s^{-1} for $z = 3.0$) return the high values of χ^2.

Fig. 7 shows all the [O II] LFs from $z = 3.0$ to the local universe $z = 0.1$ to show the LF evolution as a function of redshift. In general, the number of galaxies increases and the slope of the LFs decreases (i.e., α decreases) as a function of redshift. The number of [O II] galaxies at the lowest luminosity increases by almost 2 orders of magnitude from $z = 0.1$ to $z = 3.0$ whereas relatively small change is observed at the highest luminosity end. The LFs do not evolve much at low redshift $z < 1.0$ but strong evolution is observed at high redshift $1.0 \leqslant z \leqslant 3.0$.

Fig. 8 shows the slope α of the LFs as a function of redshift. The slopes for the bright (L([O II]) $\geqslant 10^{42.0}$ erg s^{-1}) and faint (L([O II]) $\leqslant 10^{41.2}$ erg s^{-1}) ends of the LFs are plotted against $(z + 1)^{-1}$ as squares and circles, respectively. For both ends, α

Table 1. Fitting parameters of the LFs of [OII] emitters in equations (4) and (5)

z	α_l	β_l	$\chi^2_{\rm l,red}$	α_h	β_h	L_*	$\chi^2_{\rm h,red}$
0.1	-2.21 $\pm$ 0.06	46.96 $\pm$ 2.60	1.10	-1.59 $\pm$ 0.15	-4.10 $\pm$ 0.22	43.06 $\pm$ 0.14	0.16
0.3	-2.23 $\pm$ 0.07	47.88 $\pm$ 2.90	2.16	-1.91 $\pm$ 0.13	-4.80 $\pm$ 0.34	43.40 $\pm$ 0.21	0.14
0.6	-2.10 $\pm$ 0.08	42.64 $\pm$ 3.22	3.37	-1.88 $\pm$ 0.14	-4.56 $\pm$ 0.30	43.16 $\pm$ 0.18	0.09
1.0	-2.40 $\pm$ 0.26	55.37 $\pm$ 10.77	38.03	-2.05 $\pm$ 0.11	-4.13 $\pm$ 0.34	42.98 $\pm$ 0.21	1.49
2.0	-3.15 $\pm$ 0.14	86.61 $\pm$ 5.92	37.80	-1.74 $\pm$ 0.06	-3.35 $\pm$ 0.14	42.85 $\pm$ 0.09	1.14
3.0	-2.59 $\pm$ 0.07	64.10 $\pm$ 3.07	43.42	-1.65 $\pm$ 0.08	-3.29 $\pm$ 0.11	42.96 $\pm$ 0.07	0.19

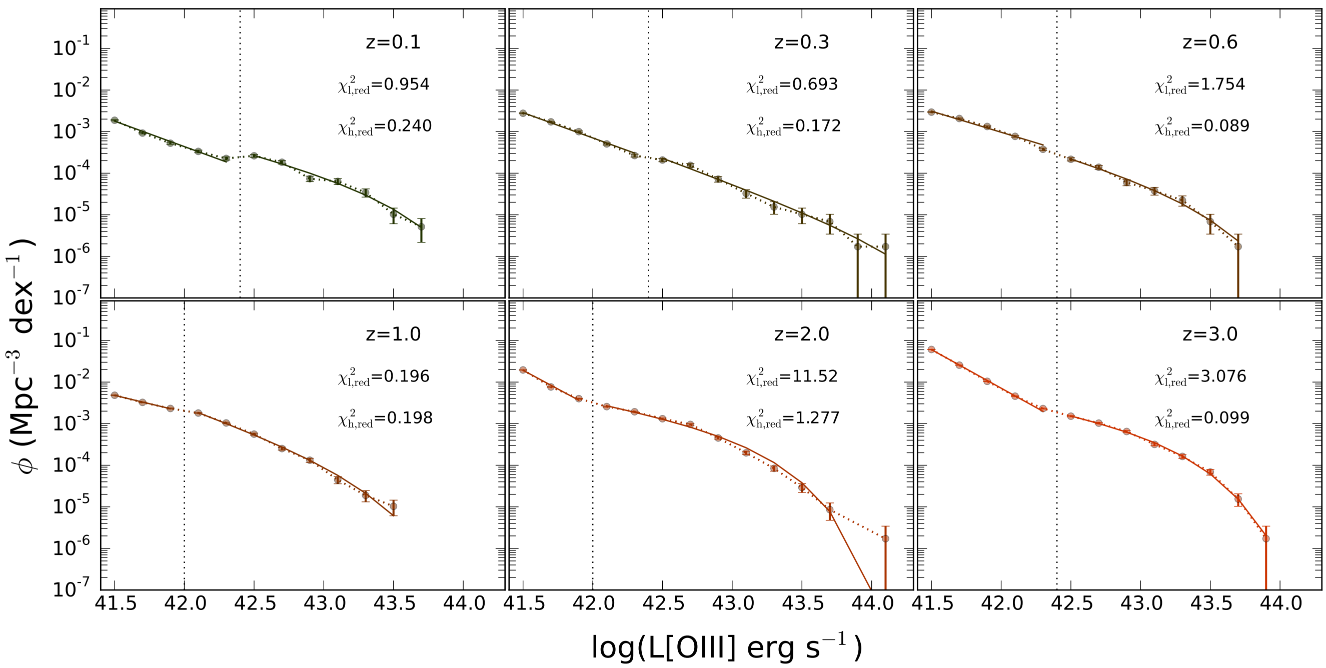

Figure 9. LFs together with fitting functions of the [O III] ELGs at $z = 0.1$, 0.3, 0.6, 1.0, 2.0, and 3.0. The [O III] LF is similar to the [O II] LF except for the fact that L([O III]) is higher than L([O II]) of a same SFR. The dotted vertical line at each redshift shows the dividing luminosity for fitting LFs at low and high luminosity.

shows a minor change at $z \leqslant 0.3$. For the bright end, the slope changes approximately as $(z+1)^{-1}$ whereas the slope of the faint end shows the bigger change approximately being proportional to $\sim 3(z+1)^{-1}$ at high redshift $0.6 \leqslant z \leqslant 2.0$. The slopes for both ends display the minima at $z = 2.0$. Since the Poisson errors dominate at the bright end of the LFs, the slopes for L([O II]) $\geqslant 10^{42.4}$ erg s^{-1} are plotted additionally (pentagons) to see how the errors affect the determination of the slopes. The number of [O II] galaxies at the highest luminosity bins L([O II]) $\sim$ $10^{43.6}$ erg s^{-1} is typically 2–3 in the simulated volume, and thus the Poisson statistics greatly affects the determination of the slopes. For a comparison with observations, the slopes from Zhu, Moustakas & Blanton (2009); Gilbank et al. (2010); Comparat et al. (2015) are plotted together in Fig. 8, however, note that their luminosity cuts do not exactly match with the ones from the current work for both bright and faint ends. For example, the luminosity range of the bright end from Gilbank et al. (2010) is $10^{41.0}$ < L([O II]) < $10^{42.5}$ erg s^{-1}. The evolution of the [O II] LF as a function of redshift is driven by the evolution of GSMF, i.e., by the cosmic SFR in different stellar masses. Thus, it is important to model the SFR in various stellar mass ranges. At low mass end, the SFR is greatly affected by the star-formation feedback model whereas the AGN feedback greatly affects the high stellar mass end.

3.3 [OIII] luminosity functions

In this section, we briefly discuss the LFs of the [O III] emitting galaxies in the MBII, since the upcoming survey WFIRST-AFTA will explore the evolution of the [O III] emission line LFs at high redshift. We repeat the process for the LFs of the [O II] emitters for [O III] emission line. In the synthesised SEDs of the star-forming galaxies, the emission-line fluxes of the [O II] and [O III] lines are calculated in a similar manner. Note that the [O III] LFs in Fig. 9 are very similar to the [O II] LFs in Fig. 6 except for the fact that the [O III] luminosity is higher than [O II]. We fit the LFs with two functions as we do for [O II] LFs; however, we split the LFs at the luminosity 0.4 dex higher than the luminosity for the [O II] at L([O III]) $=$ $10^{42.4}$ erg s^{-1}. Fig. 9 shows the [O III] LFs along with fitting functions at redshift $z = 0.1, 0.3, 0.6, 1.0, 2.0,$ and 3.0, respectively. Fig. 10 shows all the [O III] LFs at $0.06 \leqslant z \leqslant 3.0$ together; Table 2 lists the fitting parameters.

Table 2. Fitting parameters of the LFs of [OIII] emitters in equations (4) and (5)

z	α_l	β_l	$\chi^2_{\rm l,red}$	α_h	β_h	L^*	$\chi^2_{\rm h,red}$
0.1	-2.23 $\pm$ 0.08	48.10 $\pm$ 3.51	0.95	-1.90 $\pm$ 0.26	-4.43 $\pm$ 0.55	43.50 $\pm$ 0.33	0.24
0.3	-2.22 $\pm$ 0.06	47.88 $\pm$ 2.51	0.69	-2.24 $\pm$ 0.16	-5.76 $\pm$ 1.13	44.22 $\pm$ 0.71	0.17
0.6	-2.01 $\pm$ 0.08	39.57 $\pm$ 3.52	1.75	-2.01 $\pm$ 0.20	-4.55 $\pm$ 0.44	43.43 $\pm$ 0.24	0.09
1.0	-1.80 $\pm$ 0.04	30.96 $\pm$ 1.49	0.20	-2.22 $\pm$ 0.08	-4.09 $\pm$ 0.25	43.23 $\pm$ 0.13	0.20
2.0	-2.80 $\pm$ 0.18	73.08 $\pm$ 7.36	11.52	-1.67 $\pm$ 0.10	-3.24 $\pm$ 0.16	43.16 $\pm$ 0.10	1.28
3.0	-2.86 $\pm$ 0.04	75.79 $\pm$ 1.52	3.08	-1.67 $\pm$ 0.07	-3.23 $\pm$ 0.08	43.23 $\pm$ 0.05	0.10

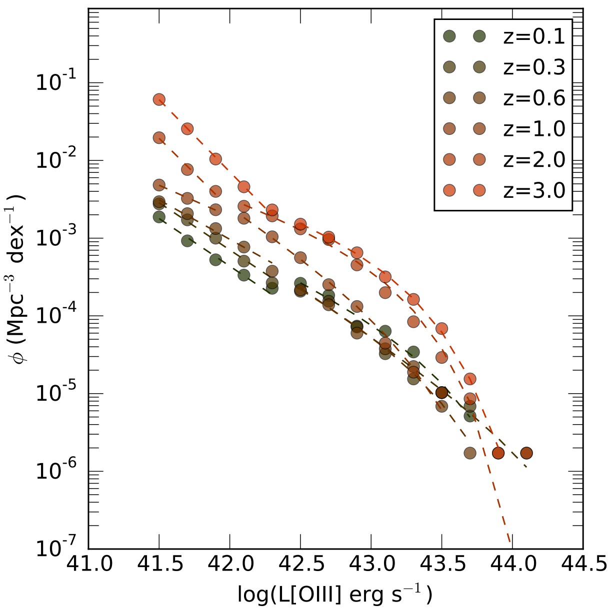

Figure 10. Evolution of LF of the [O III] emitting galaxies from $z = 3$ to $z = 0.1$. The overall shape of the [O III] LF is similar to the one for [O II] LF with a shift in luminosity.

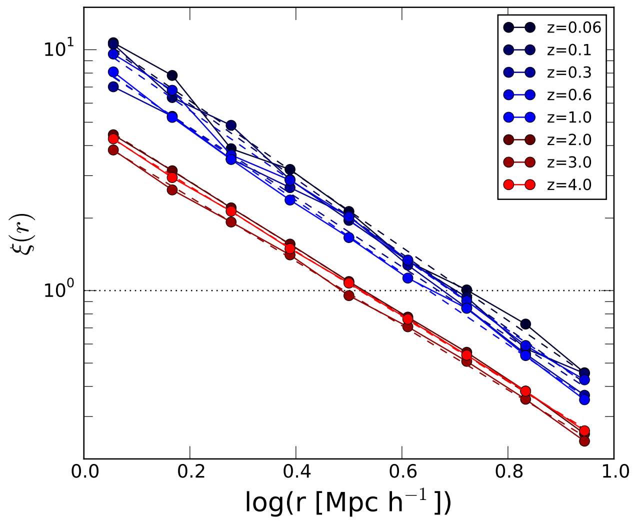

Figure 11. The auto-correlation function [ξ(r) =DD(r)/RR(r) -1] of the [O II] emitting galaxies for redshift z = 0.06, 0.1, 0.3, 0.6, 1.0, 2.0, 3.0, and 4.0. ξ shows a significant evolution from z = 2.0 to 1.0. The intersection between the power-law fitting function $\xi_{\rm fit}(r)$ (dashed) and $\xi = 1$ (dotted) shows the correlation length $l_{\rm corr}$ for each redshift.

3.4 Evolution of the auto-correlation function of [OII] emitters

In this section, using the spatial distribution of the [O II] emission-line selected galaxies, we explore the evolution of the 2-point auto-correlation function [ξ(r) =DD(r)/RR(r) -1] at $0.06 \leqslant z \leqslant 4.0$, where DD(r) is the number of galaxy pairs with separation r and RR(r) is the number of pairs with the same separation for a random (i.e., Poisson) distribution. Fig. 11 shows the auto-correlation functions of [O II] emitters at the redshifts $z = 0.06, 0.1, 0.3, 0.6, 1.0, 2.0, 3.0,$ and 4.0 along with the corresponding fitting functions shown as dashed lines. When the auto-correlation function is fitted with a power-law as $\xi_{\rm fit}(r) = (r/l_{\rm corr})^{m_{\rm corr}}$, $\xi_{\rm fit}(l_{\rm corr}) = 1$ is obtained where $l_{\rm corr}$ is the correlation length within which the galaxy distribution is correlated. In Fig. 11, the intersection between the power-law fitting function for each redshift $\xi_{\rm fit}(r)$ and $\xi = 1$ shows the correlation length $l_{\rm corr}$ for each redshift. Table 3 lists the fitting parameters of the auto-correlation functions. The ξ shows a significant evolution from $z = 2.0$ to 1.0 whereas it evolves mildly at $z \leqslant 1.0$ or $z \geqslant 2.0$. At $z \leqslant 1.0$, the slopes remain constant in the range $m_{\rm corr} = -1.55$ to -1.45 while the correlation length increases from $l_{\rm corr} = 4.47$ Mpc h^{-1} at $z = 1.0$ to $l_{\rm corr} = 5.23$ Mpc h^{-1} at $z = 0.06$. At $z \geqslant 2.0$, the slopes display slightly larger values than the ones for $z \leqslant 1.0$ in the range of $m_{\rm corr} = -1.38$ to -1.33 and the smaller correlation lengths are clearly observed in the range $l_{\rm corr} = 3.10$–3.37 Mpc h^{-1}.

Table 3. Fitting parameters of the auto-correlation functions

z	$m_{\rm corr}$	$l_{\rm corr}$ (Mpc h^{-1})
0.06	-1.52	5.23
0.1	-1.55	4.99
0.3	-1.45	4.66
0.6	-1.52	4.92
1.0	-1.50	4.47
2.0	-1.38	3.37
3.0	-1.33	3.10
4.0	-1.35	3.31

4 SUMMARY AND DISCUSSION

In this paper, we investigate the properties of the [O II] ELGs in the state-of-the-art high-resolution cosmological simulation MBII. The MBII simulates galaxies including baryonic physics for star-formation and AGN feedback in a comoving volume of $100\ h^{-1}$ Mpc on a side from $z = 159$ to $z = 0.06$. From the

synthesised SEDs of the individual galaxies, which includes the stellar continuum and the emission lines based on the star formation history, we select a sub-sample of star-forming galaxies based on the [O II] luminosity in the redshift range $0.06 \leqslant z \leqslant 3.0$. We validate the use of the extracted L([O II]) by comparing it with several observations. The MBII simulation shows a good agreement with observations, and we focus on the evolution of the [O II] (and [O III]) LFs in the redshift range $0.06 \leqslant z \leqslant 3.0$. We expect that the current work is useful for forthcoming surveys such as HETDEX, DESI, and WFIRST-AFTA. We summarise our main findings as follows.

- The specific SFR as a function of stellar mass agrees with the GAMA survey when galaxies with high [O II] luminosity are selected as L([O II]) $\geqslant 10^{41.5}$ erg s^{-1}.

- We show that the [O II] LF at $z = 1.0$ from the MBII shows a good agreement with the LFs from several surveys (Zhu, Moustakas & Blanton 2009; Comparat et al. 2015) below L([O II])=$10^{43.0}$ erg s^{-1} while the low redshifts ($z \leqslant 0.3$) show an excess in the prediction of bright [O II] galaxies, but still displaying a good match with observations (Gilbank et al. 2010; Ciardullo et al. 2013; Comparat et al. 2015) below L([O II])=$10^{41.6}$ erg s^{-1}.

- We present the LFs of [O II] and [O III] ELGs at the redshift range $0.1 \leqslant z \leqslant 3.0$ and provide fitting functions for each redshift. Each [O II] LF at different redshift is fitted with a single power-law at low luminosity (L([O II]) $\lesssim 10^{42.0}$ erg s^{-1}) while Schechter function is applied at high luminosity (L([O II]) $\gtrsim 10^{42.0}$ erg s^{-1}). In general, the LF increases and the slope of the LF also becomes steeper with increasing redshift. The slopes of the LFs at bright and faint ends range from -3 to -2 showing minima at $z = 2$. The slope of the bright end evolves approximately as $(z + 1)^{-1}$ at $z \leqslant 2$ while the faint end evolves as $\sim 3(z+1)^{-1}$ at $0.6 \leqslant z \leqslant 2$. We apply a similar analysis to the [O III] LF with a shift of 0.4 dex.

- The auto-correlation function of [OII] ELGs shows a significant evolution from $z = 2$ to 1 while it changes mildly at $z \leqslant 1$ or $2.0 \leqslant z \leqslant 4.0$. The correlation length increases from $\sim$3 Mpc h^{-1} for $z \geqslant 2$ to $\sim$5 Mpc h^{-1} for $z \leqslant 1$.

The current theoretical study of the LFs of [O II] (and [O III]) emitting galaxies will be useful for the forthcoming surveys HETDEX, DESI, and WFIRST-AFTA. The current high resolution of MBII simulations makes it possible to investigate the [O II] line of an individual galaxy and construct a better theoretical model for LFs, but the low luminosity end still suffers from shot noise. We expect that future simulations with even higher resolution can provide a solid feature at low luminosity. At the bright end of the LFs where Poisson statistics dominates, enlarging the simulation volume will help to get better errors for each luminosity bin.

The excess of galaxies at high luminosity end in [O II] (and [O III]) LF is inevitably transferred from the overabundance at the high mass end in GSMF of the MBII. In this respect, the future theoretical study of [O II] LF should be focused on the GSMF by applying observation matching star-formation and AGN feedback models. Especially at the faint end, a stronger star-formation feedback model (e.g., Okamoto et al. 2010) used in ILLUSTRIS (Vogelsberger et al. 2014) and BLUETIDES (Feng et al. 2015) can reduce the number of star-forming galaxies. On the bright end, increasing the AGN feedback (e.g., EAGLE simulation by Schaye et al. 2015) can suppress the star-formation by driving the gas out of the halos.

The dust obscuration in star-forming galaxies in low and high redshift galaxies remains as an open question. Future studies should consider the effect of dust reddening on the LF at different redshifts.

ACKNOWLEDGEMENTS

KP is supported by the Urania E. Stott Fellowship of The Pittsburgh Foundation and partly by the National Science Foundation under the Theoretical and Computational Astrophysics Network (TCAN) grant AST-1333360. TDM acknowledges the National Science Foundation, NSF Petapps, OCI-0749212 and NSF AST-1009781 for support. SH is supported by nsf-ast1412966, NASA-NNH12ZDA001N- EUCLID and doe-desc0011114. Authors thank the anonymous referee for constructive comments. Authors also thank John Wise, Edmund Hodges-Kluck, and JongHak Woo for useful comments. The numerical analysis presented in this paper was performed using the cluster facilities ("ferrari" and "coma") of the McWilliams Center for Cosmology at Carnegie Mellon University.

REFERENCES

Adams J. J. et al., 2011, ApJS, 192, 5
Anders P., Fritze-v. Alvensleben U., 2003, A&A, 401, 1063
Bauer A. E. et al., 2013, MNRAS, 434, 209
Begelman M. C., Volonteri M., Rees M. J., 2006, MNRAS, 370, 289
Blandford R. D., Netzer H., Woltjer L., Courvoisier T. J.-L., Mayor M., eds., 1990, Active Galactic Nuclei
Bondi H., 1952, MNRAS, 112, 195
Bondi H., Hoyle F., 1944, MNRAS, 104, 273
Calzetti D., 2001, PASP, 113, 1449
Chatterjee S., Degraf C., Richardson J., Zheng Z., Nagai D., Di Matteo T., 2012, MNRAS, 419, 2657
Ciardullo R. et al., 2013, ApJ, 769, 83
Colberg J. M., Di Matteo T., 2008, MNRAS, 387, 1163
Comparat J. et al., 2015, A&A, 575, A40
Croft R. A. C., Di Matteo T., Springel V., Hernquist L., 2009, MNRAS, 400, 43
DeGraf C., Di Matteo T., Khandai N., Croft R., Lopez J., Springel V., 2012, MNRAS, 424, 1892
Degraf C., Di Matteo T., Springel V., 2010, MNRAS, 402, 1927
Degraf C., Di Matteo T., Springel V., 2011, MNRAS, 413, 1383
Degraf C., Oborski M., Di Matteo T., Chatterjee S., Nagai D., Richardson J., Zheng Z., 2011, MNRAS, 416, 1591
Di Matteo T., Colberg J., Springel V., Hernquist L., Sijacki D., 2008, ApJ, 676, 33
Di Matteo T., Khandai N., DeGraf C., Feng Y., Croft R. A. C., Lopez J., Springel V., 2012, ApJ, 745, L29
Di Matteo T., Springel V., Hernquist L., 2005, Nature, 433, 604
Drory N., Feulner G., Bender R., Botzler C. S., Hopp U., Maraston C., Mendes de Oliveira C., Snigula J., 2001, MNRAS, 325, 550
Feng Y., Di Matteo T., Croft R., Khandai N., 2014, MNRAS, 440, 1865
Feng Y., Di-Matteo T., Croft R. A., Bird S., Battaglia N., Wilkins S., 2015, arXiv:1504.06619
Fioc M., Rocca-Volmerange B., 1997, A&A, 326, 950
Fioc M., Rocca-Volmerange B., 1999, arXiv:9912179

Gallego J., García-Dabó C. E., Zamorano J., Aragón-Salamanca A., Rego M., 2002, ApJ, 570, L1
Giavalisco M. et al., 2004, ApJ, 600, L93
Gilbank D. G., Baldry I. K., Balogh M. L., Glazebrook K., Bower R. G., 2010, MNRAS, 405, 2594
Heckman T. M., Kauffmann G., Brinchmann J., Charlot S., Tremonti C., White S. D. M., 2004, ApJ, 613, 109
Hopkins A. M., 2004, ApJ, 615, 209
Hopkins A. M., Beacom J. F., 2006, ApJ, 651, 142
Kennicutt R. C., Evans N. J., 2012, ARA&A, 50, 531
Kennicutt, Jr. R. C., 1989, ApJ, 344, 685
Kennicutt, Jr. R. C., 1998, ARA&A, 36, 189
Kewley L. J., Geller M. J., Jansen R. A., 2004, OJ, 127, 2002
Khandai N., Di Matteo T., Croft R., Wilkins S., Feng Y., Tucker E., DeGraf C., Liu M.-S., 2015, MNRAS, 450, 1349
Komatsu E. et al., 2011, ApJS, 192, 18
Levi M. et al., 2013, arXiv:1308.0847
Li Y. et al., 2007, ApJ, 665, 187
Lilly S. J., Le Fevre O., Hammer F., Crampton D., 1996, ApJ, 460, L1
Ly C., Malkan M. A., Kashikawa N., Hayashi M., Nagao T., Shimasaku K., Ota K., Ross N. R., 2012, ApJ, 757, 63
Ly C. et al., 2007, ApJ, 657, 738
Madau P., Ferguson H. C., Dickinson M. E., Giavalisco M., Steidel C. C., Fruchter A., 1996, MNRAS, 283, 1388
Moustakas J., Kennicutt, Jr. R. C., Tremonti C. A., 2006, ApJ, 642, 775
Netzer H., 2009, MNRAS, 399, 1907
Okamoto T., Frenk C. S., Jenkins A., Theuns T., 2010, MNRAS, 406, 208
Pelupessy F. I., Di Matteo T., Ciardi B., 2007, ApJ, 665, 107
Pierre M. et al., 2004, J. Cosmology Astropart. Phys., 9, 11
Schaye J. et al., 2015, MNRAS, 446, 521
Schechter P., 1976, ApJ, 203, 297
Schlegel D. J. et al., 2009, arXiv:0904.0468
Scoville N. et al., 2007, ApJS, 172, 1
Shakura N. I., Sunyaev R. A., 1973, A&A, 24, 337
Sijacki D., Springel V., Di Matteo T., Hernquist L., 2007, MNRAS, 380, 877
Speagle J. S., Steinhardt C. L., Capak P. L., Silverman J. D., 2014, ApJS, 214, 15
Spergel D. et al., 2013, arXiv:1305.5422
Springel V., Di Matteo T., Hernquist L., 2005, MNRAS, 361, 776
Springel V., Hernquist L., 2003, MNRAS, 339, 289
Vogelsberger M. et al., 2014, Nature, 509, 177
Volonteri M., Rees M. J., 2006, ApJ, 650, 669
Wilkins S. M., Bunker A., Coulton W., Croft R., Matteo T. D., Khandai N., Feng Y., 2013a, MNRAS, 430, 2885
Wilkins S. M. et al., 2013b, MNRAS, 435, 2885
Zhu G., Moustakas J., Blanton M. R., 2009, ApJ, 701, 86

APPENDIX A: VALIDATION OF THE [OII] LF

We compare the [O II] LFs calculated using different methods for the purpose of validation in Fig. A1. We confirm that our method recovers the intrinsic LF of the [O II] well, as shown in Fig A1. The sampling of the [O II] emitting galaxies start to lose star-forming galaxies at L([O II]) $\leqslant 10^{40.6}$erg s^{-1} due to the sensitivity of the [O II] emission line on the SF timescale and the shot noise due to the mass resolution of the gas particles in the MBII simulation.

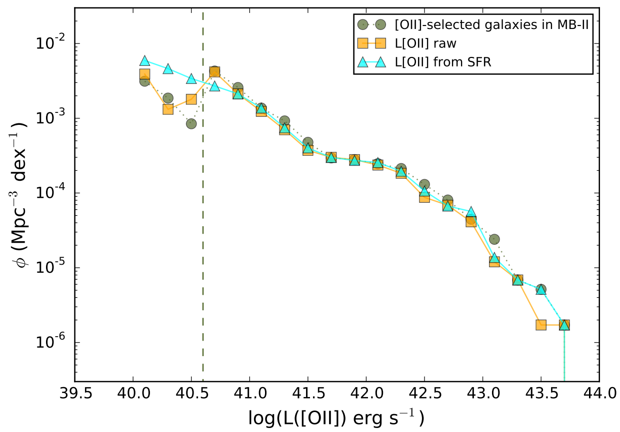

Figure A1. LFs of [O II] emitting galaxies in the MBII at $z = 0.06$. Circles show the [O II]-selected galaxies while squares show the LF of the raw L([O II]) before the emission lines are added to the stellar SEDs for each galaxy. Triangles show the LF of the L([O II]) which is converted from the SFR using the empirical relationship by Kewley, Geller & Jansen (2004). Our method of selecting [O II] ELGs recovers the LF of the intrinsic [O II] lines well. The LF starts to lose star-forming galaxies due to the fact that the [O II] lines trace the average SF history of the past ~ 20 Myr. Note that the LF converted from the SFRs keeps increasing toward the low luminosity end. Shot noise due to the mass of the star particles also starts to dominate in the low luminosity L([O II]) $< 10^{40.6}$erg s^{-1} shown as a vertical dashed line.

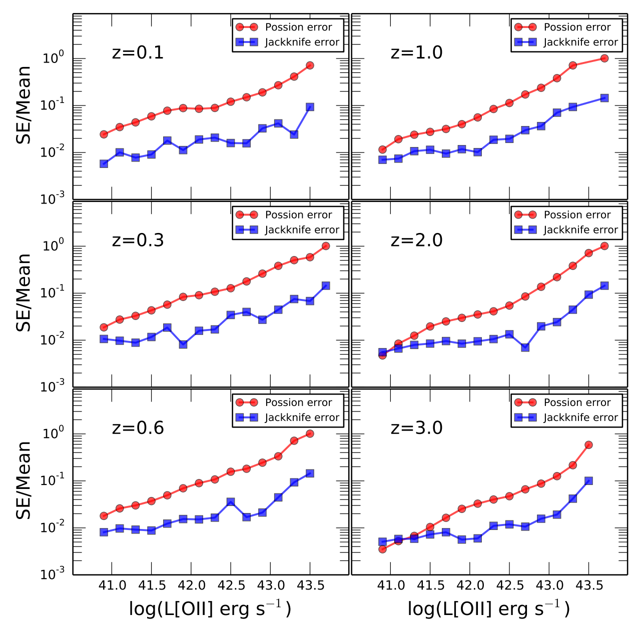

Figure A2. Comparison of Poisson and Jackknife re-sampling errors. For each luminosity bin, Poisson errors ($\sqrt{N}$) are obtained (circles) from the number of galaxies (N). Jackknife sampling of 8 cubes with comoving volume of 50 Mpc h^{-1} on a side is used to get errors due to the cosmic variance. The Poisson and Jackknife errors, shown here, are normalised by the mean value.

APPENDIX B: STANDARD ERRORS OF THE LF

We compare the errors of the LFs in each redshift from Poisson statistics and Jackknife re-sampling. Fig. A2 shows the standard errors normalised by the mean values for each luminosity bin. Poisson errors ($\sqrt{N}$) are obtained (circles) from the number of galaxies (N) in each luminosity bin. Jackknife sampling of 8 cubes with comoving volume of (50 Mpc h^{-1})^3 is used to get the errors to consider the cosmic variance. Poisson errors are bigger than the Jackknife re-sampling errors, whereas both errors are comparable at low luminosity L([O II]) $\sim 10^{41}$ erg s^{-1}.